Article

Not peer-reviewed version

Screening of Commercially Available Layers for Diffusive & Transparent Overhead Agrivoltaics: From Layer Characterization to Prototyping

Marco Memminger [*,†], Alessandro Minini [†], Jordi Veirman [*], Giovanni Borz, Martina Pelle, Valentino Diener, Damiano Adami, Lukas Koester, Alexander Astigarraga, Giampaolo Manzolini, David Moser

Posted Date: 17 April 2026

doi: 10.20944/preprints202604.1231.v1

Keywords: agrivoltaics; c-Si PV modules; diffusive properties; cosine-corrected BTDF; impact on electric performance

 doi:10.20944/preprints202604.1231.v1

Article

Screening of Commercially Available Layers for Diffusive & Transparent Overhead Agrivoltaics: From Layer Characterization to Prototyping

Marco Memminger [1,2,*,†], Alessandro Minini [1,2,†], Jordi Veirman [1,*], Giovanni Borz [1], Martina Pelle [1], Valentino Diener [1], Damiano Adami [1], Lukas Koester [1], Alexander Astigarraga [1], Giampaolo Manzolini [2] and David Moser [3]

[1] Institute for Renewable Energy, EURAC Research, Viale Druso 1, I-39100 Bolzano, Italy
[2] Dipartimento di energia, Politecnico di Milano, Via Lambruschini 4, 20156 Milano, MI, Italy
[3] Becquerel Institute Italia, Via Kufstein 5, 38121 Trento, Italy
* Correspondence: marco.memmingerbz@gmail.com (M.M.); jordi.veirman@eurac.edu (J.V.)
† These authors contributed equally to this work.

Abstract

Agrivoltaics (Agri-PV) represents a promising solution to improve land-use efficiency by simultaneously allowing crop growth and photovoltaic (PV) energy generation, with additional benefits for crop production if properly engineered. However, when crystalline silicon (c-Si) PV modules are used for Agri-PV, even in semi-transparent configurations, shading occurs over crops, potentially reducing agricultural yields. Enhancing light diffusion is a key strategy to partially compensate for this effect, as diffuse light is more efficiently utilized by most plants. This study aims at engineering the transparent section of a semi-transparent c-Si PV module, assessing its optical, light-scattering, and efficiency-related properties for Agri-PV applications. The experimental work involved fabricating and testing various transparent stack configurations and mini-module prototypes to evaluate their suitability for Agri-PV integration. Optical characterization using a spectrophotometer revealed that certain stack configurations significantly enhance light diffusion, while maintaining good transmittance values for crops growth. To further analyze angular light scattering, a custom-built setup to measure the Bidirectional Transmittance Distribution Function (BTDF) was developed. The results showed that primarily anti-glare films (AG) and secondarily specific encapsulants (TPO) and flexible layers can effectively improve light distribution, helping to mitigate shading effects. Following AG application, Haze values exceeded 89%, indicating enhanced light diffusion capabilities. The impact of different stacks on module efficiency was also assessed through mini-modules testing. Findings indicate that enhanced light diffusion can be achieved with minimal efficiency losses. Specifically, the application of the AG resulted in a reduction of the Cell-To-Module efficiency ratio (CTM_{η}) of less than 1%. These results confirm that semi-transparent PV modules can be optimized for Agri-PV applications without significantly compromising energy output.

Keywords: agrivoltaics; c-Si PV modules; diffusive properties; cosine-corrected BTDF; impact on electric performance

1. Introduction

To reduce CO2 emissions, the European Union has raised its renewable energy target to 42.5% of the overall energy mix by 2030 [1]. In this scenario, Solar PV energy is expected to double its current installed capacity by 2028 [1]. However, large-scale PV installations require vast land areas [2], leading to competition for land use with agricultural fields. A viable solution to this challenge is overhead agrivoltaics (Agri-PV), which integrates PV modules above agricultural practices, enabling the simultaneous production of food and energy. Compared to other systems, this configuration allows

 doi:10.20944/preprints202604.1231.v1

for higher protection against hail and heavy rainstorms, mitigation of overheating and better water management for the crops [3]. Yet, when c-Si PV modules (opaque in the visible wavelength range) are used in these Agri-PV systems, light availability is reduced, potentially leading to negative impacts on agricultural yields [4]. To mitigate these shading effects, semitransparency is required. In c-Si modules, this is achieved by increasing the spaces between cells and using a non-opaque back cover [5]. However, semitransparency alone is typically not sufficient: to partly compensate the shading effect, a viable solution is to increase light diffusion (i.e. scattering) at the crop canopies [5]. This is because literature findings suggest that plants utilize diffuse light more efficiently than direct light. In fact, diffuse light penetrates deeper into crop canopies, enhancing light intensity and photosynthetic capacity in the middle and lower leaves, while the top leaves exhibit similar photosynthetic behavior regardless of light diffuseness [5]. Therefore, while other design parameters, such as row spacing and clearance height, can influence crop growth in overhead systems, it is also important to evaluate the light-diffusing properties of the transparent section of a semi-transparent c-Si PV module. To the best of the authors' knowledge, the only other work investigating the scattering properties of materials used in c-Si PV modules for Agri-PV applications focused on various commercial encapsulants in glass-glass and glass-transparent backsheet symmetrical configurations (i.e. using the same encapsulant front and back) [5]. In contrast, the present work focuses on engineering the rear side of a PV module, by combining different encapsulants for the front and back side and incorporating multiple flexible and functional layers (anti-glare film), while also assessing the impact of the different combinations on the module's electrical performance.

2. Methodology

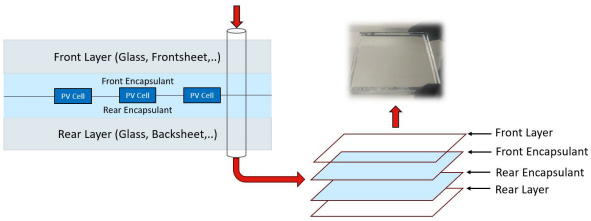

Figure 1. Transparent section of a PV module.

The focus of the work is the analysis of the transparent section (from here on renamed "stack") of a semi-transparent c-Si PV module, suitable for Agri-PV. As shown in Figure 1, it is typically composed of:

- a front layer (glass or frontsheet) with the highest possible transmittance;
- a front encapsulant, a polymeric material providing protection for the PV cells, as well as mechanical support by bonding the module layers;
- a rear encapsulant, which can be the same as the front one or a different polymeric material;
- a rear layer (glass or backsheet), which must also have a good transmittance, to allow sufficient light to reach the crops.

To perform this work, several steps were required:

1. initial selection of commercially available materials;
2. definition of the stack combinations, representative of the transparent section of the module;
3. manufacturing of several stacks as 5x5 cm samples;
4. assessment of the optical properties of these samples with a spectrophotometer;
5. analysis of the scattering features of the samples, using a custom-made set up;
6. selection of some stacks to create mini-modules: impact evaluation of different stacks on the electrical performance.

A more detailed overview of the instruments used in this work will be presented in *Section 3.1*.

 doi:10.20944/preprints202604.1231.v1

2.1. Materials Selection

Table 1. Materials used to manufacture the different stacks.

Code	Name	Type
BS	Clr HDPYE 370 1100 3/20	Backsheet
EPE1	EPE T306	Encapsulant
EPE2	EPE U307	Encapsulant
EVA	N/A	Encapsulant
FS	ClrFS PYE MONO G 1100 3/10	Frontsheet
FSA	ClrFS HDPYE 370 1020 3/20	Frontsheet
G	Extra clear glass	Glass
AG	Anti-Glare film	Functional layer
TPO1	TPO clear	Encapsulant
TPO2	TPO light green	Encapsulant
TPO3	TPO dark green	Encapsulant

The first step involved the selection of commercially available materials suitable for semitransparent Agri-PV applications, which led to the exclusion of opaque layers. As shown in Table 1, the selected materials include one type of glass, one type of backsheet, two types of frontsheets, and six different encapsulants. Additionally, a functional layer in the form of an anti-glare film (AG) was chosen for the analysis. A similar effect is also provided by one of the two frontsheets (FSA), in which the anti-glare feature is already integrated during the manufacturing process.

2.2. Combinations Definition

The primary approach in this work was to maintain the same two front layers across all stacks to ensure a consistent theoretical power output from the sun-facing side of PV modules. Consequently, apart from some exceptions, only the last two layers of the transparent section, namely the rear encapsulant and the rear layer, were varied between the stacks, as illustrated in Figure 2.

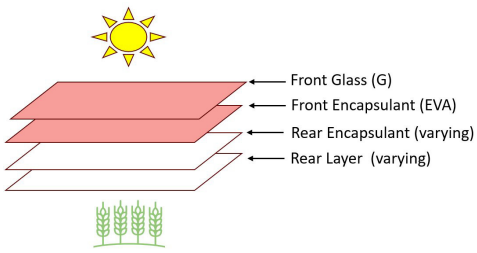

Figure 2. Layer arrangement in the analyzed stacks: for most of the samples, the front layers are G and EVA.

The selected combinations are reported in Table 2. As it can be observed, for almost all the samples Extra Clear Glass (G) was chosen as front layer, and EVA as front encapsulant. However, not all the stacks maintain the same front part composed of Glass and EVA. A few exceptions were identified as particularly interesting to investigate: combinations 1a, 62, and 63. Moreover, a distinctive aspect of this work is the unconventional use of the two frontsheets (FSA and FS), which were employed as backsheets instead of their usual position as sun-facing layers. As a result, the side of the frontsheet normally exposed to sunlight was instead oriented towards the ground.

 doi:10.20944/preprints202604.1231.v1

Table 2. List of combinations: the layer sequence is from the sun-facing to the ground-facing layer.

Sample Number	Combination Stack
0	G-EVA-EVA-G
1a	AG-G-EVA-EVA-G
1b	G-EVA-EVA-G-AG
2	G-EVA-EVA-BS
6	G-EVA-EVA-FSA
8	G-EVA-EVA-FS
10	G-EVA-EPE1-G
12	G-EVA-EPE1-BS
16	G-EVA-EPE1-FSA
18	G-EVA-EPE1-FS
20	G-EVA-EPE2-G
22	G-EVA-EPE2-BS
26	G-EVA-EPE2-FSA
28	G-EVA-EPE2-FS
30	G-EVA-TPO1-G
32	G-EVA-TPO1-BS
36	G-EVA-TPO1-FSA
38	G-EVA-TPO1-FS
40	G-EVA-TPO2-G
42	G-EVA-TPO2-BS
46	G-EVA-TPO2-FSA
48	G-EVA-TPO2-FS
50	G-EVA-TPO3-G
52	G-EVA-TPO3-BS
56	G-EVA-TPO3-FSA
58	G-EVA-TPO3-FS
62	G-TPO1-TPO1-G
63	AG-G-EVA-EVA-G-AG

2.3. Optical Characterization: Transmittance and Haze

The primary objective of this analysis was to compute the Haze for the selected combinations. Therefore, the Spectral Total Transmittance (τ_T) and Spectral Diffuse Transmittance (τ_D) of the investigated samples were first measured using a spectrophotometer, as illustrated in *Section 3.3*. These spectral properties were then used to compute the Global Total Transmittance (T_T) and the Global Diffuse Transmittance (T_D) using a weighted average approach. Given that both the spectral transmittance and the incident irradiance are available at discrete wavelengths, the integrals were numerically approximated using the trapezoidal rule:

$$T \approx \frac{\sum_{i=1}^{n-1} \frac{\tau_i \cdot S_i + \tau_{i+1} \cdot S_{i+1}}{2} \cdot \Delta\lambda_i}{\sum_{i=1}^{n-1} \frac{S_i + S_{i+1}}{2} \cdot \Delta\lambda_i}, \tag{1}$$

where τ_i and S_i represent the spectral transmittance (either total or diffuse) and the reference spectral incident irradiance at wavelength λ_i, respectively. The term $\Delta\lambda_i$ denotes the wavelength step between successive measurements, while n is the total number of discrete wavelength points considered in the summation. In this study, the spectral irradiance data S_i used for the calculation corresponds to the AM 1.5 hemispherical solar spectrum, as defined by ASTM G173-03 [6]. Haze, in accordance with ASTM D1003-21 [7], is defined as:

$$Haze = \frac{T_D}{T_T} \cdot 100\ [\%] \tag{2}$$

 doi:10.20944/preprints202604.1231.v1

For this study, it was computed over the Photosynthetically Active Radiation (PAR) range (400–700 nm) [5], which is crucial for plant growth and fruits yield. Haze serves as a preliminary metric for assessing the scattering potential of different sample configurations. However, it lacks information on the directionality of the scattered radiation, calling for further analysis to achieve a more complete optical characterization.

2.4. Scattering Analysis: BTDF and ARS

To complement the Haze analysis, Cosine-Corrected Bidirectional Transmittance Distribution Function (BTDF) measurements were conducted using a custom-made setup, to assess the angular distribution of transmitted light. The BTDF was measured discretely along a single plane of the transmittance hemisphere and assumed the following finite form [8,9]:

$$BTDF(\theta_t) = \frac{E_t(\theta_t)}{E_i \cdot \Omega_d \cdot \cos(\theta_t)} \ [sr^{-1}], \tag{3}$$

where $E_t(\theta_t)$ represents the transmitted irradiance at the transmission angle θ_t, E_i is the incident irradiance, and Ω_d is the solid angle collected by the detector. In this study, E_i was always approximately normal to the surface of the samples. Moreover, the spectral contributions from E_t and E_i were integrated over the PAR range to obtain a single BTDF value representative of the entire interval, rather than multiple spectral values. To remove the cosine correction factor, which can artificially amplify scattering at high transmission angles [10], the cosine-corrected BTDF or Angle-Resolved Scattering (ARS) function for the transmittance hemisphere is introduced:

$$ARS(\theta_t) = \frac{E_t(\theta_t)}{E_i \cdot \Omega_d} \ [sr^{-1}] \tag{4}$$

To further assess the spatial homogeneity of scattered radiation, the Relative ARS (ARS_R) was computed as:

$$ARS_R(\theta_t) = \left(\frac{ARS(\theta_t)}{ARS(\theta_t = 0°)} \right) [\%] \tag{5}$$

The ARS_R quantifies how quickly the transmitted irradiance decreases with an increasing transmission angle. Given that the most relevant energy contribution falls within $\theta_t = 0°$ to $\theta_t = 15°$, the ARS_R at $\theta_t = 15°$ was chosen as a metric for light distribution uniformity.

2.5. Electrical Analysis

As previously mentioned, some combinations (1a, 62, and 63) feature a modified sun-facing side with respect to the reference sample (0), potentially leading to differences in the power output contribution of the front side compared to the rest of the batch. At the same time, the use of bifacial cells in large-scale Agri-PV plants is steadily increasing [2]. Given the variation in the rear-side materials among the analyzed stacks, the rear power output will also vary among the different combinations. For these reasons, an analysis on the impact of the different layers on the module efficiency was conducted in this study. 10 combinations were selected from the original list of 28 samples for mini-module manufacturing. The goal was to include at least one mini-module for each encapsulant and each front/back layer.

3. Experimental Activity

3.1. Instruments Employed

Several instruments were used in this experimental work, as reported in Figure 3.

 doi:10.20944/preprints202604.1231.v1

Device	Device Name and Description
	**a)**: Spectrophotometer by *Agilent Technologies*. Used for assessing the optical spectral properties of the stacks.
	**b)**: Laminator by *Tecno Panamac* (SL-DM121). Used for the lamination process, sealing the different layers of the stacks. It operates under vacuum conditions, with a maximum pressure difference of 1 bar and a maximum temperature of 180 °C.
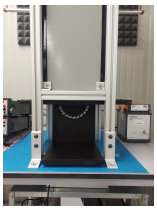	**c)**: Customized experimental setup for light scattering measurements. It comprises of three different devices: • Sun Simulator by *G2V Optics* (Sunbrick™); • custom-built scattering analysis device; • spectrometer by *Avantes*.
	**d)**: Flash Simulator by *Pasan SA*. Used for I-V curve measurements of PV solar cells and mini-modules under Standard Test Conditions (STC).

Figure 3. Instruments employed in the experimental activity.

3.2. Lamination

The layers constituting the selected combinations were cut, assembled, and laminated using a Tecno Panamac laminator. Generally, lamination recipes consist of the following steps:

1. **Pre-heating**: The assembled stacks are placed in the laminator, where the bottom surface is preheated to 50°C.
2. **Vacuuming (Degassing)**: The laminator is closed, and air is evacuated to remove trapped air bubbles between the layers.
3. **Heating and Pressurization**: The temperature is increased to 130–160°C (depending on the selected lamination recipe), causing the encapsulant to soften and melt. Pressure is gradually applied (up to 500–700 mbar) to ensure proper adhesion. Due to the laminator characteristics, temperature and pressure do not increase simultaneously (i.e., when temperature increases, pressure remains steady, and vice versa), requiring multiple steps. Once the target temperature and pressure are reached, they are maintained for 10–20 minutes (curing phase). In this stage, EVA and EPE undergo a cross-linking reaction, forming stable covalent bonds between polymer chains. In contrast, TPO does not cross-link: it adheres through physical bonding driven by thermal processing [11]. This curing phase ensures long-term structural and chemical stability of the encapsulants under environmental stress.
4. **Cooling**: The laminated samples are cooled using circulating cooling water inside the laminator, reducing their temperature to 80–90°C. Afterwards, the laminator is opened, and the cooling process continues with ambient air.

The lamination recipes were developed according to the guidelines provided by the polymeric materials suppliers. This procedure resulted in transparent samples measuring 5×5 cm.

3.3. Optical Analysis with the Spectrophotometer

The Spectral Total Transmittance (τ_T) and Spectral Diffuse Transmittance (τ_D) were measured using a spectrophotometer by Agilent equipped with a Diffuse Reflectance Accessory (DRA), which includes an integrating sphere. The built-in light source of this instrument emits a collimated beam that

 doi:10.20944/preprints202604.1231.v1

strikes the sample surface at approximately normal incidence. Therefore, the influence of varying the incident angle was not assessed in this study. The measurement procedure is schematically illustrated in Figure 4 [12] and consists of the following steps:

- τ_T is measured with the sample placed at the entrance of the integrating sphere and a reflective plate at the exit to capture all the transmitted light.
- The sample and instrument spectral diffuse transmittance (τ_S) is measured with an open rear port, collecting only scattered radiation from both the sample and the instrument.
- The equipment-induced scattering (τ_E) is quantified by leaving both entrance and exit ports open.
- τ_D, which accounts only for light scattered by the sample itself, is computed as:

$$\tau_D = \tau_S - \tau_E \tag{6}$$

From the geometric dimensions of the integrating sphere, the DRA Critical Angle ($\gamma_t \approx 4.16°$) relative to the normal at the sample center was computed . This angle defines the threshold between specular and diffuse components of transmitted light.

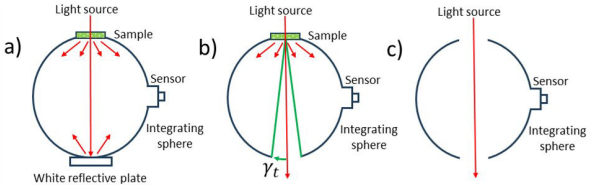

Figure 4. Spectral diffuse and total transmittance measurement steps for a sample: (a) τ_T measurement; (b) τ_S measurement and DRA Critical Angle γ_t; (c) τ_E measurement.

3.4. ARS Measurements

The measurements were conducted using a custom-built setup. A G2V Sun Simulator (Figure 5a) provided a controlled light source, while an optical fiber-based spectrometer by Avantes was used to detect the incident and transmitted irradiance. The optical fiber, equipped with a cosine corrector, was mounted on a fixing system to enable angular measurements (Figure 5b). The transmitted irradiance was measured at discrete transmission angles (θ_t) ranging from -75° to +75° at 15° intervals. The Sun Simulator LEDs emit light at angles below 30°, and its highly reflective internal walls could cause the incident irradiance to reach the samples from multiple directions. To mitigate this, an opaque metallic cylinder with a diameter of 1 cm was introduced to block highly angular incident radiation, ensuring that only near-normal irradiance reaches the samples. This prevents the overestimation of diffusive properties in highly transmissive samples.

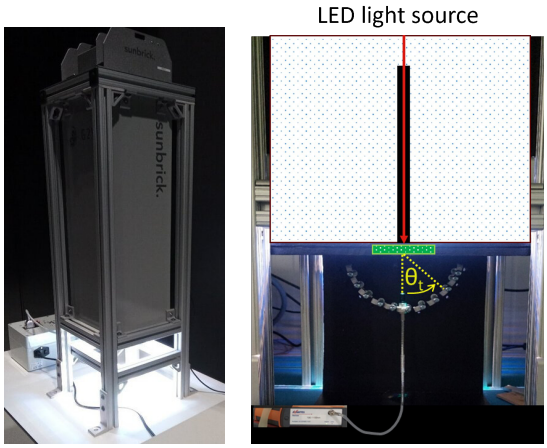

Figure 5. G2V Sun Simulator (a) and a sectioned view with the fiber fixing system and the opaque metallic cylinder (b).

 doi:10.20944/preprints202604.1231.v1

While the opaque cylinder effectively limits highly angular incident radiation, it also introduces a secondary issue: spatial inhomogeneity in the incident irradiance. The restricted aperture modifies the way the LEDs emissions interact, preventing them from effectively superimposing at the base of the sun simulator. As a result, the irradiance at the upper surface of the samples exhibits significant variations in intensity depending on fiber positioning. The combined uncertainty in ARS measurements was estimated by accounting for the uncertainties in E_t, E_i, and Ω_d (see *Eq.* 4). Regarding E_t, the uncertainty was estimated through repeated measurements while replacing both the fiber and the samples. The total uncertainty was calculated using the Root Sum of Squares (RSS) method, following standard error propagation rules for independent measured quantities [13]. As a result, an uncertainty in the ARS values of up to 10% can be expected.

3.5. Electrical Impact Assessment

To assess the impact of the different stacks on the electrical performance, the following steps were conducted:

1. measurements of the I-V curve of the bare PV cells in the module Flash Simulator;
2. lamination of the PV cells with specific layer combinations (Table 3) to create mini-modules (23×23 cm, single-cells);
3. measurements of the I-V curves of the complete mini-modules. An example is shown in Figure 6.

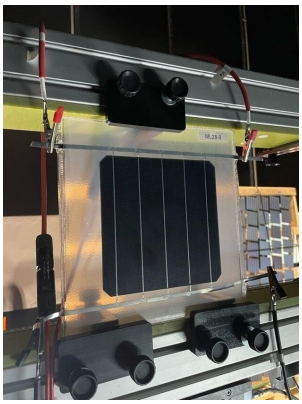

Figure 6. Mini-module I-V curve measurement.

The PV cells used in this study are based on PERC technology [14] and are monofacial, meaning that they feature only one active side. Therefore, to evaluate the impact of sun-facing layers on modules efficiency, the cells were placed with their usual orientation, with the active side facing the light source. Since nearly all samples share the same front-side configuration, mini-module 0, comprising glass and EVA on both front and back, is considered representative of the sun-facing performance for most configurations (Figure 7). Conversely, to investigate the impact of rear-side layers on module efficiency (mini-modules 2 to 56), the cells were deliberately placed in a reversed orientation, with the active side facing the rear layers, as shown in Figure 8.

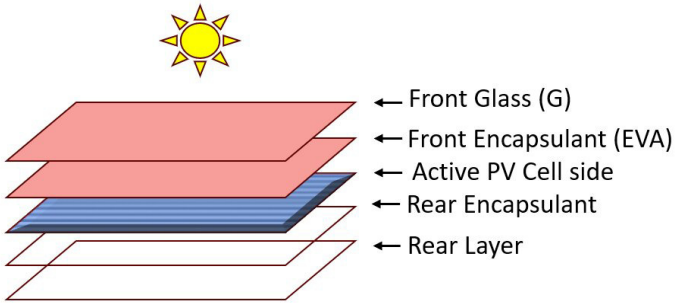

Figure 7. Front-side efficiency test.

 doi:10.20944/preprints202604.1231.v1

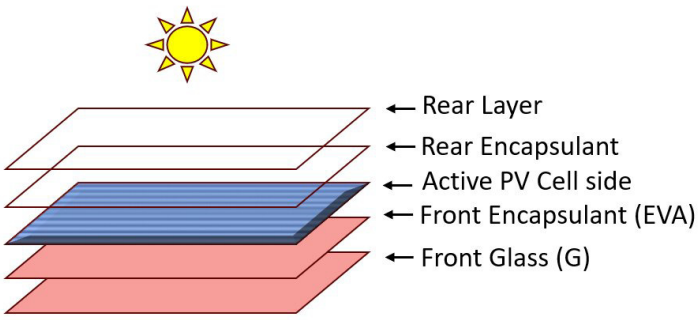

Figure 8. Rear-side efficiency test.

Table 3. Selected stacks for mini-modules fabrication. The first material mentioned in each name is facing the light source. Manufacturing of combinations highlighted in red failed.

N°	Mini-Module Composition
0	**G-EVA-Cell**-EVA-G
1	**AG-G-EVA-Cell**-EVA-G
2	**BS-EVA-Cell**-EVA-G
6	**FSA-EVA-Cell**-EVA-G
8	**FS-EVA-Cell**-EVA-G
40	**G-TPO2-Cell**-EVA-G
50	**G-TPO3-Cell**-EVA-G
52	**BS-TPO3-Cell**-EVA-G
56	**FSA-TPO3-Cell**-EVA-G
62	**G-TPO1-Cell**-TPO1-G

Not all the mini-modules were laminated together: depending on the specific encapsulants, different lamination recipes were used, and several lamination runs were needed. Not all configurations were successfully fabricated (see Table 3, highlighted in red): the EVA-TPO3-flexible layer combinations (modules 52 and 56) failed due to unresolved compatibility issues in the lamination process, resulting in significant bubbles formation. This indicates that full modules with these configurations could not yet be reliably manufactured in the laboratory.

From the I-V curves measurements, the efficiencies of bare cells (η_c) and of the corresponding mini-modules (η_m) were extracted and the CTM$_\eta$ was derived for each combination as:

$$CTM_\eta = \frac{\eta_m}{\eta_c} \tag{7}$$

This parameter provides an immediate indication of the extent to which the layers covering the cells influence their efficiencies.

4. Results and Discussion

4.1. Transmittance and Haze

Figure 9 presents the τ_T and τ_D measurements for three selected samples: the reference sample (0), the same sample with the AG applied on the front side (1a), and a sample featuring TPO as the sole encapsulant (62). Sample 1a exhibits enhanced spectral scattering, whereas the reference sample shows minimal diffusion. The small discontinuity that appears around 800 nm for sample 1a is caused by a light source change in the spectrophotometer. This measurement artifact affected multiple sample combinations, but no clear material-level correlation was identified. In contrast to sample 1a, the sole TPO-based stack (sample 62) displays a pronounced wavelength dependence for τ_D, with higher values at shorter wavelengths followed by a gradual decline beyond 350 nm. This strong spectral sensitivity is consistent with Rayleigh scattering theory [15], which is typically associated with the presence of inhomogeneities that are much smaller than the wavelength of the incident light. Furthermore, the TPO-based sample demonstrates greater UV transparency than EVA, while the AG

 doi:10.20944/preprints202604.1231.v1

effectively blocks UV radiation. This distinction is particularly relevant, given that UV radiation can significantly influence crops growth [16]. Moreover, UV exposure also has detrimental effects on the performance of PV cells [17]. Consequently, UV-transparent modules may experience a gradual reduction in power output over time due to increased UV-induced degradation. On the other hand, UV-absorbing encapsulants, while offering protection to PV components, can themselves degrade, leading to discoloration (e.g. yellowing) and a loss in transmittance, which also negatively affects power generation [18]. This highlights the importance of balancing UV management strategies to optimize both agricultural benefits and photovoltaic efficiency. In this work, the UV Cutoff Wavelength ($\lambda_{UV,cut}$) was defined as the value of λ at which τ_T falls below 10%, in accordance with [19].

Table 4. Global Total Transmittance (T_T) and Haze values in the PAR range for the analyzed samples. The UV cutoff wavelengths ($\lambda_{UV,cut}$) are also included.

Sample	T_T PAR	Haze PAR	$\lambda_{UV,cut}$ [nm]
0_G-EVA-EVA-G	89%	1%	328
1a_AG-G-EVA-EVA-G	85%	91%	384
1b_G-EVA-EVA-G-AG	76%	89%	386
2_G-EVA-EVA-BS	82%	23%	386
6_G-EVA-EVA-FSA	76%	86%	388
8_G-EVA-EVA-FS	78%	53%	392
10_G-EVA-EPE1-G	89%	2%	326
12_G-EVA-EPE1-BS	82%	19%	386
16_G-EVA-EPE1-FSA	76%	86%	388
18_G-EVA-EPE1-FS	77%	56%	392
20_G-EVA-EPE2-G	89%	2%	350
22_G-EVA-EPE2-BS	83%	19%	386
26_G-EVA-EPE2-FSA	76%	85%	388
28_G-EVA-EPE2-FS	77%	55%	392
30_G-EVA-TPO1-G	86%	15%	344
32_G-EVA-TPO1-BS	79%	25%	386
36_G-EVA-TPO1-FSA	73%	87%	388
38_G-EVA-TPO1-FS	72%	57%	392
40_G-EVA-TPO2-G	82%	18%	346
42_G-EVA-TPO2-BS	74%	28%	388
46_G-EVA-TPO2-FSA	69%	87%	390
48_G-EVA-TPO2-FS	71%	41%	392
50_G-EVA-TPO3-G	82%	34%	346
52_G-EVA-TPO3-BS	75%	44%	388
56_G-EVA-TPO3-FSA	70%	89%	390
58_G-EVA-TPO3-FS	70%	69%	392
62_G-TPO1-TPO1-G	85%	25%	304
63_AG-G-EVA-EVA-G_AG	75%	96%	390

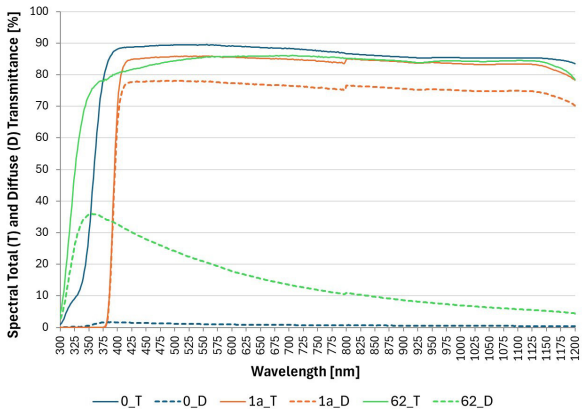

Figure 9. Spectral Total Transmittance (τ_T, continuous lines) and Spectral Diffuse Transmittance (τ_D, dotted lines) as a function of Wavelength for samples 0, 1a and 62.

 doi:10.20944/preprints202604.1231.v1

Table 4 reports the values of $\lambda_{UV,cut}$ for the various samples, along with T_T and Haze results in the PAR range. It is worth recalling that, in this work, Haze refers to the percentage of transmitted light scattered by more than 4.16° relative to the normal to the samples surface. Sample 0 displays the highest transmittance (89%) but minimal Haze (1%), due to the G-G structure and the use of EVA, characterized by high transmittance and low scattering properties [5], as the sole encapsulant. The AG enhances scattering in samples 1a, 1b, and 63, all showing Haze values above 89%, albeit with reduced transmittance. Moreover, front-side application (1a) outperforms rear-side placement (1b), yielding higher transmittance (85% vs. 76%) and Haze (91% vs. 89%). This is because the AG was specifically designed for application on the front side of PV modules installed near airports or residential areas to reduce glare. As a result, a lower transmittance is expected when the AG is applied to the rear side. Among the flexible rear layers, the FSA, featuring an AG matt, provides the most pronounced enhancement in light scattering. Regarding the encapsulants, TPOs outperform EVA in terms of Haze, as previously reported by Asa'a et al. [5], who observed Haze values up to 80% for a glass–double TPO–transparent BS configuration. In the present study, the Dark-Green TPO (TPO3), showed the most pronounced effect. The performance of TPO-based samples could be further enhanced by optimizing the cooling process, as literature findings indicate that natural air convection cooling yields better Haze properties compared to pressed cooling [20]. Finally, EPE-based samples (10 to 28) did not show significant improvements over EVA and were therefore excluded from ARS measurements.

4.2. ARS

To improve readability, Figure 10 presents the ARS trends only for a selected subset of samples, expanding on the Haze analysis by providing directional information about the scattered radiation, which is essential for a complete assessment of light distribution. Overall, ARS decreases significantly, by up to multiple orders of magnitude, as the Transmission Angle (θ_t) increases. This indicates that most of the transmitted energy remains concentrated in the specular direction, particularly between $\theta_t = 0°$ and $\theta_t = 15°$. Samples with lower Haze values, such as the reference combination (0), tend to exhibit higher ARS at $\theta_t = 0°$, in line with the definition of Haze. In contrast, samples incorporating the AG layer (dotted lines: 1a, 1b, and 63) display broader and more uniform scattering profiles.

Figure 11 compares ARS_R at $\theta_t = 15°$ with T_T. In this context, T_T is a key factor, as it quantifies the total transmitted light, independent of samples scattering properties. While diffused light benefits crops, maintaining an adequate transmittance is of utmost importance in overhead Agri-PV applications, where c-Si cells obstruct a significant part of the incoming light. Among the analyzed combinations, sample 1a emerges as a balanced solution, achieving high scattering uniformity ($ARS_R \approx 46\%$ for $\theta_t = 15°$) with a transmittance loss of approximately 4% compared to sample 0. In contrast, sample 63 demonstrates the highest scattering potential ($ARS_R \approx 60\%$ for $\theta_t = 15°$) but at the cost of a substantial reduction in transmittance, which is approximately 14% lower than that of sample 0.

The selection of an optimal configuration ultimately depends on specific Agri-PV parameters, including crop type, module height, and cells spacing [2].

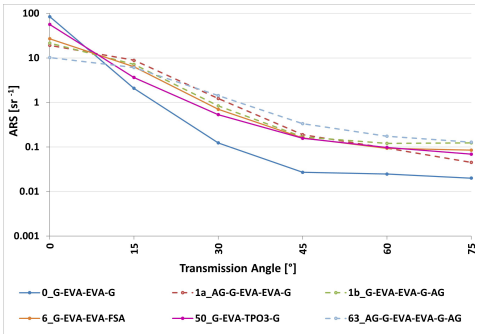

Figure 10. ARS (semi-logarithmic plot) as a function of positive Transmission Angles (θ_t): comparison between different solutions. The samples featuring the AG layer are reported as dotted lines. An uncertainty of up to 10% in the ARS values is expected.

 doi:10.20944/preprints202604.1231.v1

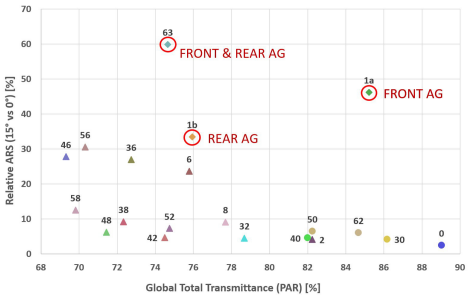

Figure 11. Relative ARS ($\theta_t = 15°$) compared to Global Total Transmittance (T_T) for all samples (combinations numbers reported). G-G samples are represented as circles, G-Flexible Layer samples as triangles and samples featuring the AG as diamonds. The red circles highlight the effects of AG application on sample 0.

4.3. Impact on Efficiency

Table 5. CTM$_\eta$ for the analyzed combinations.

Mini-Module Composition	CTMη
0_G-EVA-Cell-EVA-G	93.46 %
1_AG-G-EVA-Cell-EVA-G	92.76 %
2_BS-EVA-Cell-EVA-G	91.44 %
6_FSA-EVA-Cell-EVA-G	91.40 %
8_FS-EVA-Cell-EVA-G	92.99 %
40_G-TPO2-Cell-EVA-G	93.93 %
50_G-TPO3-Cell-EVA-G	93.82 %
62_G-TPO1-Cell-TPO1-G	95.89 %

Table 5 presents the key results of the electrical impact assessment, showing the CTM$_\eta$ ratios for the different mini-modules. The most notable observations are as follows:

- Overall, the CTM$_\eta$ variations among different mini-modules are relatively small, with a maximum CTM$_\eta$ ratio difference of less than 5% (between combinations 62 and 6).
- Compared to the standard technology (0), all EVA-EVA mini-modules (1, 2, 6, 8) show slightly lower CTM$_\eta$ ratios, with the highest deficits observed for BS (2) and FSA (6) combinations, probably due to a lower total transmittance. However, it is important to emphasize that these results cannot be directly correlated with the optical analysis, as no measurements were performed in both testing directions, nor were half-stack combinations considered.
- 0.7% CTM$_\eta$ ratio reduction observed for the AG (mini-module 1) compared to the reference solution, highlighting the fact that this layer has little effect on the efficiency while improving significantly light scattering.
- Higher CTM$_\eta$ ratios for combinations 40, 50 and 62. This is likely due to TPO high UV transparency, combined with the capacity of PERC cells to effectively utilize UV photons for current generation [21]. Combination 62 shows the highest CTM$_\eta$ ratio, presumably due to a higher total transmittance.

It is also important to note that, due to the specific protocol adopted, the results obtained can be used to estimate the expected power output of real Agri-PV systems for any combination of bifaciality factor and albedo.

5. Conclusions

This work evaluated the light scattering potential of various material combinations representative of the transparent area of semitransparent c-Si Agri-PV modules. An optical characterization consisting of Haze and ARS measurements assessed light diffusion, while electrical tests evaluated their impact on modules performance. The ARS analysis confirmed the trends observed in Haze measurements, identifying the AG as the most effective material at enhancing scattering with minimal

 doi:10.20944/preprints202604.1231.v1

transmittance loss. Front-side application outperformed rear-side placement in transmittance (T_T, 85% vs. 76%) and Haze (91% vs. 89%), while also exhibiting more homogeneous scattering (Relative ARS difference over 10%). The dark-green TPO (TPO3) improved diffusion compared to EVA and other TPO variants, whereas flexible rear layers, particularly FSA, further enhanced scattering but at the cost of transmittance. Efficiency tests showed that the AG had a minimal impact on the CTM_η ratio (less than 1% loss with respect to the reference sample), while TPO encapsulants enhanced it, with combination 62 achieving a CTM_η increase of over 2%. On the other hand, flexible rear layers led to larger efficiency reductions. The optimal solution, while inherently case-dependent, must balance total light transmission and diffusion. Future work includes:

- implementing Hortiscatter measurements [22] (possible with more advanced equipment) would provide a more comprehensive metric, capable of capturing light behavior at various incident angles rather than only at 0°, as done in this study. This would offer an additional criteria for material selection;
- performing long-term material reliability and UV degradation tests [23] on full modules, followed by repeated optical characterizations to verify that transmittance and scattering properties are preserved over time;
- developing simulations and full-scale Agri-PV tests to assess macroscopic diffusion effects.

Full-scale semi-transparent modules based on some of the assessed combinations (e.g. 0, 1a and 30) have been succesfully manufactured at Eurac Research PV Prototyping Lab (Figure 12). These modules will be implemented in a pilot Agri-PV system at the same location to evaluate the tangible effects of various levels of transmissivity and diffusivity on crops growth and fruits yield.

Figure 12. Full-scale semitransparent module based on configuration 1a.

Author Contributions: **Marco Memminger** & **Alessandro Minini** (equal): conceptualization, data curation, formal analysis, investigation, methodology, software, validation, visualization, writing-original draft preparation. **Jordi Veirman**: conceptualization (equal), funding aquisition (support), investigation (support), methodology (support), project administration (lead), resources (lead), supervision (lead), writing-review & editing (lead). **Giovanni Borz** & **Martina Pelle** (support): resources, supervision, writing-review & editing. **Valentino Diener** & **Damiano Adami** (support): resources. **Lukas Koester** & **Alexander Astigarraga** (support): investigation. **Giampaolo Manzolini** (support): conceptualization, supervision, writing-review & editing. **David Moser**: conceptualization (support), funding aquisition (lead).

Funding: This study was developed in the framework of the research activities carried out within the Project "Network 4 Energy Sustainable Transition—NEST", Spoke 1., Project code PE0000021, funded under the National Recovery and Resilience Plan (NRRP), Mission 4, Component 2, Investment 1.3 — Call for tender No. 1561 of 11.10.2022 of Ministero dell'Universita' e della Ricerca (MUR); funded by the European Union—NextGenerationEU. Also, it is included in the research project: "nuovi Concetti, mAteriali e tecnologie perl'iNtegrazione del foto-VoltAico negli edifici in uno scenario di generazione diffuSa" [CANVAS], funded by the Italian Ministry of the

 doi:10.20944/preprints202604.1231.v1

Environment and the Energy Security, through the Research Fund for the Italian Electrical System (type-A call, published on G.U.R.I. n. 192 on 18-08-2022).

Data Availability Statement: The data supporting the findings of this study are available from the corresponding author upon reasonable request.

Acknowledgments: The authors would like to thank Juan Jose' Stivanello and Gabriella Gonnella for providing their support to this work. This study was developed in the framework of the research activities carried out within the Project "Network 4 Energy Sustainable Transition—NEST", Spoke 1., Project code PE0000021, funded under the National Recovery and Resilience Plan (NRRP), Mission 4, Component 2, Investment 1.3 — Call for tender No. 1561 of 11.10.2022 of Ministero dell'Universita' e della Ricerca (MUR); funded by the European Union—NextGenerationEU. Also, it is included in the research project: "nuovi Concetti, mAteriali e tecnologie perl'iNtegrazione del fotoVoltAico negli edifici in uno scenario di generazione diffuSa" [CANVAS], funded by the Italian Ministry of the Environment and the Energy Security, through the Research Fund for the Italian Electrical System (type-A call, published on G.U.R.I. n. 192 on 18-08-2022).

Conflicts of Interest: The authors declare no conflicts of interest.

Acronyms and Symbols

The following abbreviations are used in this manuscript:

AM	Air Mass
ARS	Angle Resolved Scattering [sr^{-1}]
ARS$_R$	Relative ARS [%]
Agri-PV	Agrivoltaics
BTDF	Bidirectional Transmittance Distribution Function [sr^{-1}]
CTM$_\eta$	Cell-To-Module efficiency ratio [%]
c-Si	Crystalline-Silicon
DRA	Diffuse Reflectance Accessory
G-G	Glass-Glass
PAR	Photosynthetically Active Radiation
PERC	Passivated Emitter and Rear Contact
PV	Photovoltaic
RSS	Root Sum of Squares
STC	Standard Test Conditions
γ_t	DRA Critical Angle [°]
η_c	Cell efficiency [%]
θ_t	Transmission Angle [°]
λ	Wavelength [nm]
$\lambda_{UV,cut}$	UV Cutoff Wavelength [nm]
τ	Spectral Transmittance [%]
τ_D	Spectral Diffuse Transmittance [%]
τ_E	Spectral Diffuse Transmittance, equipment [%]
τ_S	Spectral Diffuse Transmittance, sample and equipment [%]
τ_T	Spectral Total Transmittance [%]
Ω_d	Detector Solid Angle [°]
E_i	Incident Irradiance [$\frac{W}{m^2}$]
E_t	Scattered Transmitted Irradiance [$\frac{W}{m^2}$]
S	Reference AM 1.5 Solar Spectrum
T	Global Transmittance [%]
T_D	Global Diffuse Transmittance [%]
T_T	Global Total Transmittance [%]

 doi:10.20944/preprints202604.1231.v1

References

1. de Falco, M.; Sarrica, M.; Scognamiglio, A.; Fasanelli, R. What does Agrivoltaics means? A study on social representations shared by experts and the press in Italy. *Energy Research & Social Science* **2025**, *119*, 103918. https://doi.org/https://doi.org/10.1016/j.erss.2024.103918.
2. S. Asa, T. Reher, J.R.J.D.J.P.H.R.A.v.d.H.B.V.d.P.M.D. A multidisciplinary view on agrivoltaics: Future of energy and agriculture. *Renewable and Sustainable Energy Reviews* **2024**, *200*, 114515.
3. Semeraro, T.; Scarano, A.; Curci, L.M.; Leggieri, A.; Lenucci, M.; Basset, A.; Santino, A.; Piro, G.; De Caroli, M. Shading effects in agrivoltaic systems can make the difference in boosting food security in climate change. *Applied Energy* **2024**, *358*, 122565. https://doi.org/https://doi.org/10.1016/j.apenergy.2023.122565.
4. Katsikogiannis, O.A.; Ziar, H.; Isabella, O. Integration of bifacial photovoltaics in agrivoltaic systems: A synergistic design approach. *Applied Energy* **2022**, *309*, 118475. https://doi.org/https://doi.org/10.1016/j.apenergy.2021.118475.
5. Asa'a, S.N.; Bizinoto Ferreira Bosco, G.; Kyranaki, N.; van der Heide, A.; Sivaramakrishnan Radhakrishnan, H.; Poortmans, J.; Daenen, M. Assessing the light scattering properties of c-Si PV module materials for agrivoltaics: Towards more homogeneous light distribution in crop canopies. *Solar Energy* **2024**, *276*, 112690.
6. ASTM International. ASTM G173-03(2020), Standard Tables for Reference Solar Spectral Irradiances: Direct Normal and Hemispherical on 37° Tilted Surface. Accessed Online: 2025-02-06.
7. ASTM International. ASTM D1003-21, Standard Test Method for Haze and Luminous Transmittance of Transparent Plastics, 2021. Accessed Online: 2025-02-05.
8. Wang, H.; Zheng, X.; Du, W. Automatic measurement of spectral bidirectional transmittance distribution function on translucent optical materials. *Measurement* **2015**, *69*, 126–133.
9. Stover, J.; of Photo-optical Instrumentation Engineers, S., Optical Scattering: Measurement and Analysis; Press Monographs, SPIE Optical Engineering Press, 1995; pp. 20–22.
10. Schröder, S.; von Finck, A.; Duparré, A. Standardization of light scattering measurements. *Advanced Optical Technologies* **2015**, *4*, 361–375.
11. Fiandra, V.; Sannino, L.; Andreozzi, C.; Flaminio, G.; Pellegrino, M. New PV encapsulants: assessment of change in optical and thermal properties and chemical degradation after UV aging. *Polymer Degradation and Stability* **2024**, *220*, 110643. https://doi.org/https://doi.org/10.1016/j.polymdegradstab.2023.110643.
12. JASCO. Haze Value Measurement using a UV-Visible Spectrophotometer. URL https://jascoinc.com/applications/haze-measurement-uvvisible-spectrophotometer/. Accessed Online: 2025-02-05.
13. University of North Carolina-Department of Physics and Astronomy. Measurement and Uncertainty Analysis Guide, 2025. Pages 24-27. Available online: https://users.physics.unc.edu/~deardorf/uncertainty/UNCguide.pdf, Accessed: 2025-02-22.
14. Wang, Q.; Guo, K.; Gu, S.; Huang, W.; Peng, H.; Wu, W.; Ding, J. Electrical Performance, Loss Analysis, and Efficiency Potential of Industrial-Type PERC, TOPCon, and SHJ Solar Cells: A Comparative Study. *Progress in Photovoltaics: Research and Applications* **2024**, *32*, 889–903. https://doi.org/https://doi.org/10.1002/pip.3839.
15. Tabar, R.J.; Murray, C.T.; Stein, R.S. The effect of particle size on the haze of polymer films. *Journal of Polymer Science: Polymer Physics Edition* **1983**, *21*, 831–833. https://doi.org/https://doi.org/10.1002/pol.1983.180210512.
16. Jadidi, M.; Mumivand, H.; Nia, A.E.; Shayganfar, A.; Maggi, F. UV-A and UV-B combined with photosynthetically active radiation change plant growth, antioxidant capacity and essential oil composition of *Pelargonium graveolens*. *BMC Plant Biology* **2023**, *23*, 555. https://doi.org/10.1186/s12870-023-04556-6.
17. Sinha, A.; Qian, J.; Moffitt, S.L.; Hurst, K.; Terwilliger, K.; Miller, D.C.; Schelhas, L.T.; Hacke, P. UV-induced degradation of high-efficiency silicon PV modules with different cell architectures. *Progress in Photovoltaics: Research and Applications* **2023**, *31*, 36–51. https://doi.org/https://doi.org/10.1002/pip.3606.
18. Pinochet, N.; Couderc, R.; Therias, S. Solar cell UV-induced degradation or module discolouration: Between the devil and the deep yellow sea. *Progress in Photovoltaics: Research and Applications* **2023**, *31*, 1091–1100. https://doi.org/https://doi.org/10.1002/pip.3725.
19. International Electrotechnical Commission IEC. IEC 62788-1-4:2016-09+AMD1:2020-10, Measurement procedures for materials used in photovoltaic modules –Part 1-4: Encapsulants – Measurement of optical transmittance and calculation of the solarweighted photon transmittance, yellowness index, and UV cut-off wavelength, 2020. Accessed Online: 2025-06-24.
20. Meslier, Vincent.; Chambion, Bertrand.; Boulanger, Amandine.; Rahmoun, Ichrak.; Chabuel, Fabien.; Bejat, Timea. Effect of the cooling rate on encapsulant's crystallinity and optical properties, and photovoltaic modules' lifetime. *EPJ Photovolt.* **2023**, *14*, 2. https://doi.org/10.1051/epjpv/2022028.

 doi:10.20944/preprints202604.1231.v1

21. Singh, A.; Umakanth, V.; Tyagi, N.; Baghel, A.K.; Kumar, S. Comparative study of commercial crystalline solar cells. *Results in Optics* **2023**, *11*, 100379. https://doi.org/https://doi.org/10.1016/j.rio.2023.100379.
22. NEN. Greenhouse glass - Determination of optical properties of greenhouse covering materials and screens. URL https://www.nen.nl/en/nen-2675-c1-2018-en-251294. Accessed Online: 2025-06-30.
23. International Electrotechnical Commission IEC. IEC IEC-61215-1-2021, Terrestrial photovoltaic (PV) modules – Design qualification and type approval – Part 1: Test requirements, 2021. Accessed Online: 2025-06-30.